Nano Research
2022, 15(1): 535–541

ISSN 1998-0124 CN 11-5974/O4
https://doi.org/10.1007/s12274-021-3513-x

Research Article

An aqueous 2.1 V pseudocapacitor with MXene and V-MnO_2 electrodes

Jiabin Wu[1,2], Qun Li[1], Christopher E. Shuck[2], Kathleen Maleski[2], Husam N. Alshareef[3], Jun Zhou[1], Yury Gogotsi[2] (✉), and Liang Huang[1] (✉)

[1] *Wuhan National Laboratory for Optoelectronics, Huazhong University of Science and Technology, Wuhan 430074, China*
[2] *Department of Materials Science and Engineering and A. J. Drexel Nanomaterials Institute, Drexel University, Philadelphia, Pennsylvania 19104, USA*
[3] *Materials Science and Engineering, Physical Science and Engineering Division, King Abdullah University of Science and Technology (KAUST), Thuwal 23955-6900, Saudi Arabia*

Received: 21 March 2021 / **Revised:** 3 April 2021 / **Accepted:** 8 April 2021

ABSTRACT

MXenes have shown record-breaking redox capacitance in aqueous electrolytes, but in a limited voltage window due to oxidation under anodic potential and hydrogen evolution under high cathodic potential. Coupling $Ti_3C_2T_x$ MXene negative electrode with RuO_2 or carbon-based positive electrodes expanded the voltage window in sulfuric acid electrolyte to about 1.5 V. Here, we present an asymmetric pseudocapacitor using abundant and eco-friendly vanadium doped MnO_2 as the positive and $Ti_3C_2T_x$ MXene as the negative electrode in a neutral 1 M Li_2SO_4 electrolyte. This all-pseudocapacitive asymmetric device not only uses a safer electrolyte and is a much less expensive counter-electrode than RuO_2, but also can operate within a 2.1 V voltage window, leading to a maximum energy density of 46 Wh/kg. This study also demonstrates the possibility of using MXene electrodes to expand the working voltage window of traditional redox-capable materials.

KEYWORDS

MXene, pseudocapacitors, metal oxides, supercapacitors, manganese oxide

1 Introduction

The demand for safe, efficient, and environmentally friendly electrochemical energy storage devices has led to extensive research into supercapacitors (SCs) because of their high-power density, rapid charge and discharge rates, and long cycling stability [1–4]. Most common carbon-based electrochemical double-layer capacitors (EDLCs) have low energy density resulting from their electrostatic charge storage mechanism [5–8]. One approach to increase the energy density is to take advantage of pseudocapacitive materials, which store charge by reversible surface redox reactions [9–13]. The most widely used active pseudocapacitive materials are transition metal oxides [14–19], and conducting polymers [20–23]. Among these electrode materials, MnO_2 is desirable for supercapacitor applications because it has a high theoretical capacitance, coupled with its abundance, low cost, and sustainable production [24–26]. However, most efforts have been primarily devoted to improving the performance of MnO_2 as an anode material, while finding a suitable pseudocapacitive cathode material that matches well with MnO_2 has not yielded promising candidates. For a cathode to be suitable for use with a MnO_2 anode, it should be stable under negative potentials in a neutral electrolyte. Metal oxides and activated carbons are frequently used as matching negative materials in asymmetric pseudocapacitors with MnO_2 [27–29]. Nevertheless, metal oxides suffer from poor cycling stability and low electronic conductivity, limiting the power density and cyclability of SCs [7]. Activated carbons are highly conductive and can steadily operate under a wide voltage window, but their capacitance is significantly lower than that of MnO_2, owing to the EDLC charge storage mechanism and low density leading to moderate volumetric performance [30]. From this viewpoint, coupling MnO_2 with a suitable negative material that operates in a neutral electrolyte and has a high volumetric capacitance under negative potential could lead to safe and efficient energy storage devices.

MXenes are a large class of two-dimensional (2D) transition metal carbides, nitrides and carbonitrides, which demonstrate great potential as promising cathode materials for SCs. Their high conductivity ensures rapid electron transfer, large available surface area offers numerous ion accessible diffusion channels, and the abundant surface functional groups enable fast reversible redox for enhanced energy storage [31, 32]. As the first reported and most extensively studied MXene [33], titanium carbide ($Ti_3C_2T_x$; T_x refers to the surface terminations such as F, OH, and O) [34] is useful in a variety of applications including supercapacitors [35–38] and lithium-ion batteries [39–43]. $Ti_3C_2T_x$, like MnO_2, is synthesized from abundant, low-cost materials, and can be scalably produced [44, 45]. The $Ti_3C_2T_x$ vacuum-filtered films exhibit a high metallic conductivity, exceeding 10,000 S/cm in thin films, with a packing density of ~ 4 g/cm^3, leading to a high rate capability and remarkable volumetric capacitance (1,000–1,500 F/cm^3) [38, 46, 47]. For example, $Ti_3C_2T_x$ hydrogel exhibited a capacitance of 380 F/g

Address correspondence to Huang Liang, huangliang421@hust.edu.cn; Yury Gogotsi, gogotsi@drexel.edu

in 3 M H_2SO_4 up to −1.1 V vs. Hg/Hg_2SO_4 [47]. Considering this development, several asymmetric SCs were assembled using $Ti_3C_2T_x$ negative electrodes and conducting polymers or RuO_2 positive electrodes using acidic electrolytes [16, 19, 48, 49]. However, the operating voltage of these devices is limited to ~ 1.5 V due to the low overpotential for the hydrogen evolution in acidic electrolyte [16]. In this context, a neutral electrolyte can effectively broaden the working voltage window, and further improve the energy density.

Herein, we present an asymmetric pseudocapacitor with vanadium doped MnO_2 (V-MnO_2) as the positive electrode, $Ti_3C_2T_x$ as the negative electrode, and Li_2SO_4 as the electrolyte. The V-MnO_2 was chosen due to significant enhancement of the electronic conductivity of MnO_2 after V doping, as we previously demonstrated [50]. As expected, this asymmetric SC exhibits a high operating voltage of 2.1 V with a corresponding energy density of 46 Wh/kg.

2 Results and discussion

Figure 1 illustrates the design of the asymmetric supercapacitor with V-MnO_2 and $Ti_3C_2T_x$ as the positive and negative, respectively. Hydrothermal synthesis of V-MnO_2 followed previous work using NH_4VO_3 as the dopant (Fig. 1(a)) [50]. $Ti_3C_2T_x$ was synthesized using the HF/HCl method (Fig. 1(b)) [49]. Figure 1(c) displays the voltage windows of V-MnO_2 and $Ti_3C_2T_x$ tested in a three-electrode system in Li_2SO_4. The wide range of operating voltage windows shows the potential in using these materials for asymmetric devices. Figure 1(d) is the schematic representation of the all-pseudocapacitive asymmetric device where $Ti_3C_2T_x$ and V-MnO_2 are the negative and positive, respectively.

The morphologies of these materials were investigated by scanning electron microscopy (SEM) and transmission electron microscopy (TEM). The SEM and TEM images of $Ti_3C_2T_x$ show the 2D morphology of this material (Figs. 2(a) and 2(b)). The cross-section image of $Ti_3C_2T_x$ nanosheets in the assembled free-standing film demonstrates a stacked structure (Fig. 2(c)). The TEM image of V-MnO_2 shows a nanoflower morphology composed of nanosheets (Fig. 2(d)) and the high-angle annular dark-field scanning transmission electron microscopy (HAADF-STEM) mapping indicates that V is uniformly distributed in this sample (Fig. 2(e)). The phase composition of these samples was characterized using X-ray diffraction (XRD). As shown in Fig. 2(f), the XRD pattern of the MXene indicates pure $Ti_3C_2T_x$ phase without any MAX residue [44]. The XRD pattern of V-MnO_2 sample reveals tetragonal phase α-MnO_2 (JCPDS-44-0141) [50]. V doping significantly altered the morphology and supported the tunnel structure of MnO_2 and improved the electrical conductivity. The α-MnO_2 model with (2 × 2) tunnels was employed for the crystal structure of V-interstitial α-MnO_2 (Fig. S1 in the Electronic Supplementary Material (ESM)). Moreover, the Raman spectrum of V-MnO_2 shows a Raman band at 637 cm^{-1}, suggesting a tetragonal structure with an interstitial space consisting of (2 × 2) tunnels from the α-MnO_2 phase (Fig. S2 in the ESM) [50]. Fourier transform infrared (FT-IR) spectra of these two materials are presented in Fig. 2(g). The FT-IR spectrum of V-MnO_2 nanosheets shows broad bands at 3,460 and 1,647 cm^{-1} that are assigned to the stretching and bending vibrations of H_2O. Various bands from 400 to 800 cm^{-1} are attributed to the Mn–O bonds [50]. As can be seen from the FT-IR spectrum of $Ti_3C_2T_x$, the band at 1,657, 1,465 and 1,086 cm^{-1} is attributed to C=O, O–H and C–F, respectively, related to the surface functionalization of $Ti_3C_2T_x$ [51]. In addition, X-ray photoelectron spectroscopy (XPS) was employed to study the chemical composition of as-prepared samples (Figs. S3 and S4 in the ESM). As shown in Figs. 2(h) and 2(i), the peaks at 455.7 and 457.2 eV in the Ti 2p spectrum of $Ti_3C_2T_x$ are assigned to Ti–C, and C–Ti–O, respectively [52]. The peaks at 517 and 524.2 eV in the V 2p spectrum of V-MnO_2 are assigned to the V $2p_{3/2}$ and V $2p_{1/2}$, suggesting successful V-doping [50].

The electrochemical performance of these two materials was evaluated in a three-electrode configuration using Li_2SO_4 as the aqueous neutral electrolyte. The cyclic voltammetry (CV) curves of $Ti_3C_2T_x$ film in 1 M Li_2SO_4 aqueous solution could operate in a wide negative potential range from −1.2 to 0.2 V (vs. Ag/AgCl). The CV curves show a pair of weak redox peaks around −0.6 V (vs. Ag/AgCl) due to the reversible intercalation/deintercalation of Li^+ (Fig. 3(a)). The galvanostatic charge–discharge (GCD) profiles of $Ti_3C_2T_x$ exhibited a triangular shape with Coulombic efficiencies of nearly 100% from 1 to 20 A/g current density, suggesting highly reversible capacitive behavior (Fig. 3(b)). The specific capacitance of this film was 273 F/g at 5 mV/s. Increasing the scan rate to 500 mV/s, a specific capacitance of 155 F/g was maintained, illustrating a high-rate capacity of $Ti_3C_2T_x$ (Fig. 3(c)). It can be further improved by optimizing the electrode architecture [32, 53].

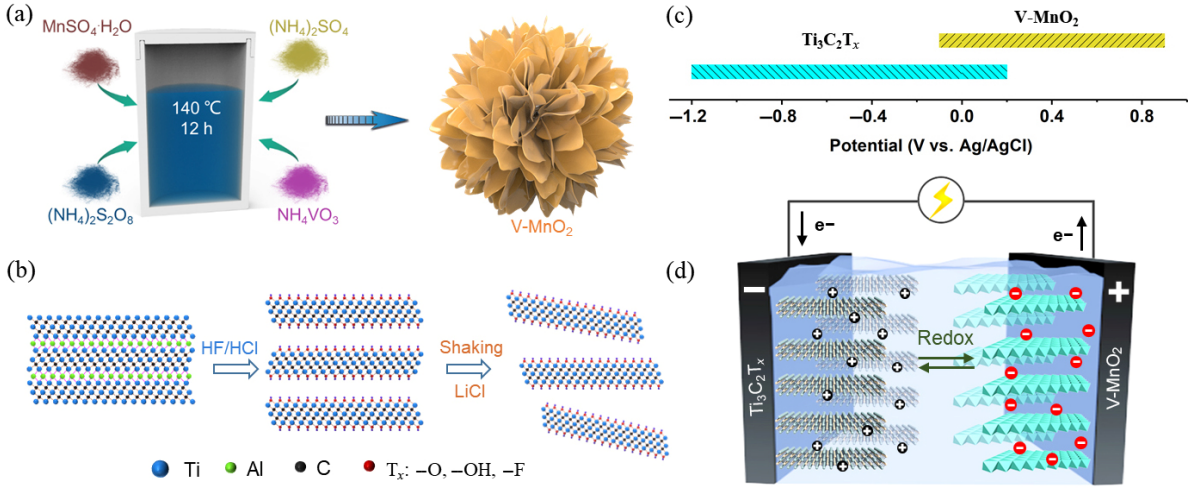

Figure 1 Fabrication process of V-MnO_2 and $Ti_3C_2T_x$ MXene and schematic illustration of the all-pseudocapacitive asymmetric supercapacitor. (a) and (b) Synthesis scheme of V-MnO_2 and $Ti_3C_2T_x$ MXene. (c) The working potential window of $Ti_3C_2T_x$ and V-MnO_2 in a three-electrode aqueous electrolyte system. (d) Schematic representation of all-pseudocapacitive asymmetric supercapacitor in which V-MnO_2 and $Ti_3C_2T_x$ serve as the positive and negative electrode, respectively.

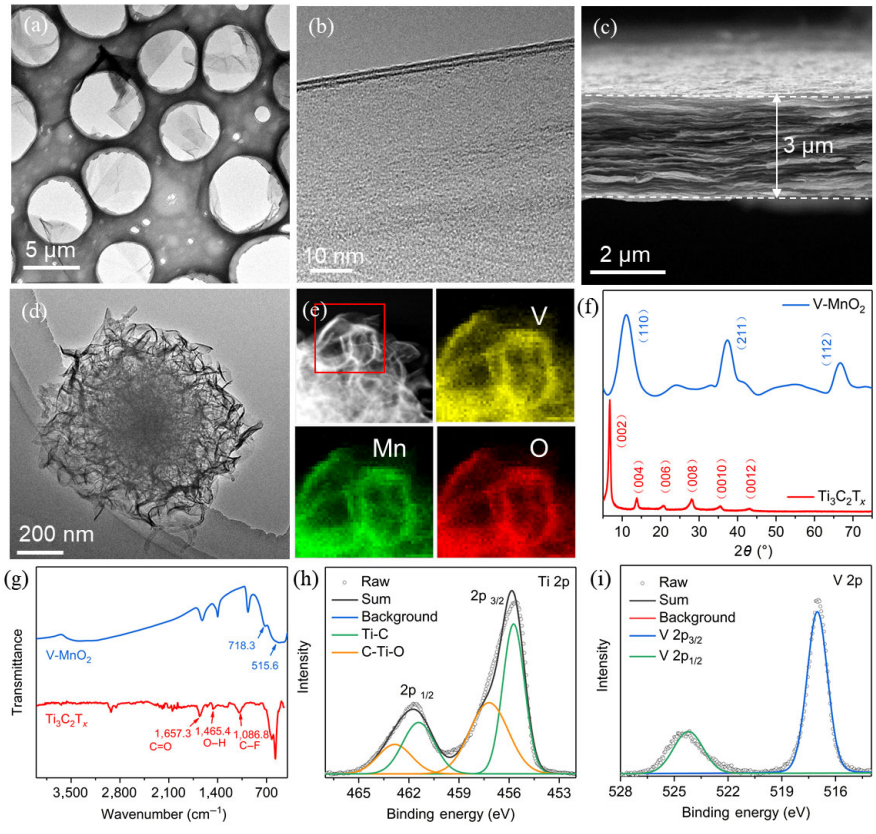

Figure 2 (a) The TEM images of $Ti_3C_2T_x$ MXene. (b) The high-resolution cross-section TEM image of $Ti_3C_2T_x$ MXene. (c) Cross-sectional SEM image of $Ti_3C_2T_x$ film. (d) TEM image of V-MnO_2. (e) The HAADF-STEM mapping of V-MnO_2. (f) The XRD patterns of $Ti_3C_2T_x$ film and V-MnO_2 powder. (g) FT-IR spectra of $Ti_3C_2T_x$ and V-MnO_2. (h) and (i) High-resolution Ti 2p and V 2p XPS spectra of $Ti_3C_2T_x$ and V-MnO_2, respectively.

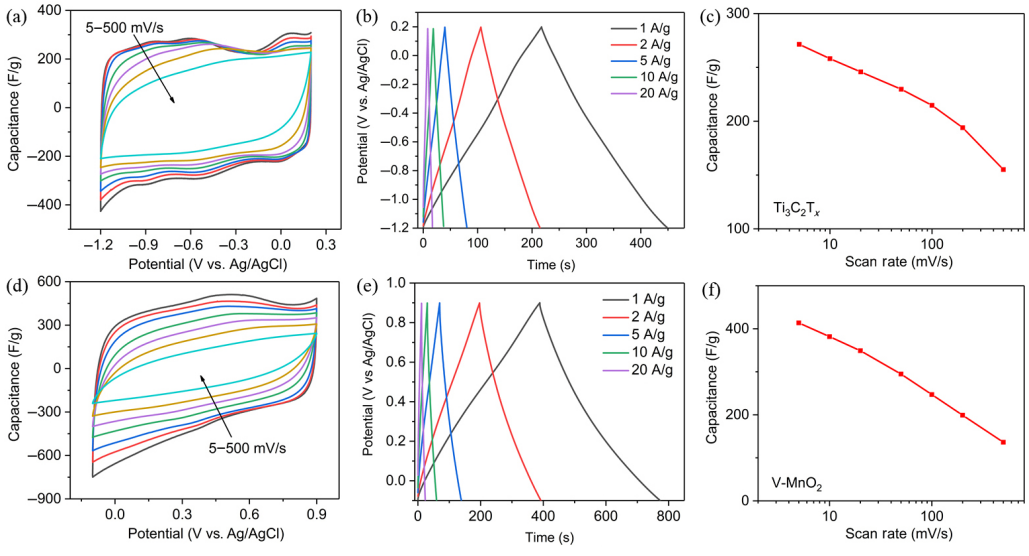

Figure 3 CV curves (a), galvanostatic charge–discharge (b), and specific capacitance at different scan rates (c) of $Ti_3C_2T_x$. CV curves (d), galvanostatic charge–discharge (e), and specific capacitance at different scan rates (f) of V-MnO_2/CNT. The electrolyte is 1 M Li_2SO_4.

The V-MnO_2 based electrode was prepared by mixing V-MnO_2 (70 wt.%) and carbon nanotube (30 wt.%, CNT) in 50 mL DI water, followed by 1-h ultrasonication and a vacuum filtration process to obtain a free-standing hybrid film (V-MnO_2/CNT). The cross-section SEM image of V-MnO_2/CNT film with a thickness of 20 μm is presented in Fig. S5 in the ESM. The electrochemical performance was also measured in three-electrode cell with 1 M Li_2SO_4. The V-MnO_2/CNT positive demonstrated reversible capacitive behavior from −0.1 to 0.9 V (vs. Ag/AgCl) as well as triangular GCD profiles (Figs. 3(d) and 3(e)). The specific capacitance of V-MnO_2/CNT at a 5 mV/s scan rate is 414 F/g, and reduces to 136 F/g when increasing the scan rate to 500 mV/s (Fig. 3(f)). These results show that the V-MnO_2/CNT and $Ti_3C_2T_x$ are well-matched negative and positive electrodes in a Li_2SO_4 electrolyte.

We constructed an asymmetric supercapacitor using V-MnO_2/CNT as the positive electrode and $Ti_3C_2T_x$ film as the negative electrode. A plastic Swagelok cell was used as the testing setup for all electrochemical measurements (Fig. S6 in the ESM). According to the CV test results in the three-electrode configuration, the $Ti_3C_2T_x$ and V-MnO_2 based electrodes exhibit a stable potential window between −1.2 and 0.2 V and between

−0.1 and 0.9 V (vs. Ag/AgCl), respectively. Because of the individual positive and negative potential windows, the operating voltage of this asymmetric SC cell is expected to extend to 2.1 V. As shown in Fig. 4(a), the asymmetric SC device demonstrated a stable electrochemical voltage window of 2.1 V without any water splitting peaks (Fig. S7 in the ESM). As far as we know, 2.1 V is the highest voltage of MXene devices in aqueous electrolytes. The CV curves of this device exhibited rectangular shapes at all measured scan rate, with a weak pair of redox peaks at 1.5–1.8 V, representative of the capacitive behavior with fast charge and discharge characteristics (Fig. 4(b)). The remarkable electrochemical performance was further studied by the GCD profiles, showing a linear relationship of charge/discharge voltage with time (Fig. 4(c)). The maximum specific capacitance of this cell is 76 F/g based on the total mass of V-MnO_2 and $Ti_3C_2T_x$, at a scan rate of 5 mV/s (Fig. 4(d)). This device retained 53% of its capacitance when the scan rate was increased from 5 to 200 mV/s.

To understand the electrochemical behavior of this device, we separated the contributions to the charge storage of the diffusion controlled and surface controlled processes [54]. As shown in Fig. 4(e), the calculated surface-capacitive contribution is ~ 79% of the total charge storage at 5 mV/s, revealing the main capacitive behavior of this device for charge storage (Fig. 4(e)). The surface-capacitive contribution gradually increased when increasing the scan rate (Fig. 4(f)). Electrochemical impedance spectroscopy (EIS) measurements were conducted to detect the electrochemical behavior of the device. The Nyquist plot of this device shows a nearly vertical line at low frequency, suggesting primarily capacitive behavior. The diameter of the quasi-semicircle at high frequency with a resistance of 2.8 Ω indicates the fast charge transfer in the device (Fig. S8 in the ESM). The real (C') and imaginary (C'') capacitances of this device were extracted from the EIS spectra and plotted as a function of frequency (Fig. 4(g)). The relaxation time constant (τ_0) of this asymmetric SC was calculated to be 177 ms. This device delivers an energy density of 46 Wh/kg. This value is higher than the reported MXene based asymmetric SCs such as MXene-RuO_2 (29 Wh/kg), MXene-conducting polymer (17 Wh/kg), and rGO//$Ti_3C_2T_x$ with LiBr additive (34.4 Wh/kg) [10, 13, 19], and MnO_2 based asymmetric SCs such as MnO_2/CNTs/graphene//CNTs/AC (29 Wh/kg), PANi/CNTs/graphene//graphene (41.5 Wh/kg), MnO_2/CNTs//CNTs (42 Wh/kg), and MnO_2//CNTs (47.4 Wh/kg). Even at the power density of 3.2 kW/kg, this cell still released an energy density of 36 Wh/kg. These results show that MXenes are promising cathodic materials, and have the potential to replace carbon-based materials for high-energy asymmetric SCs. The cycling stability is another key factor to evaluate the practical potential of this device. The long-term cycling performance of the asymmetric SC device was investigated, as shown in Fig. 4(i). The asymmetric SC achieved a specific capacitance retention of 88.6% after 10,000 cycles at 50 mV/s, indicating the stable nature of both the positive and negative. Moreover, the Coulombic efficiency of this device maintained nearly 100% during the cycling test.

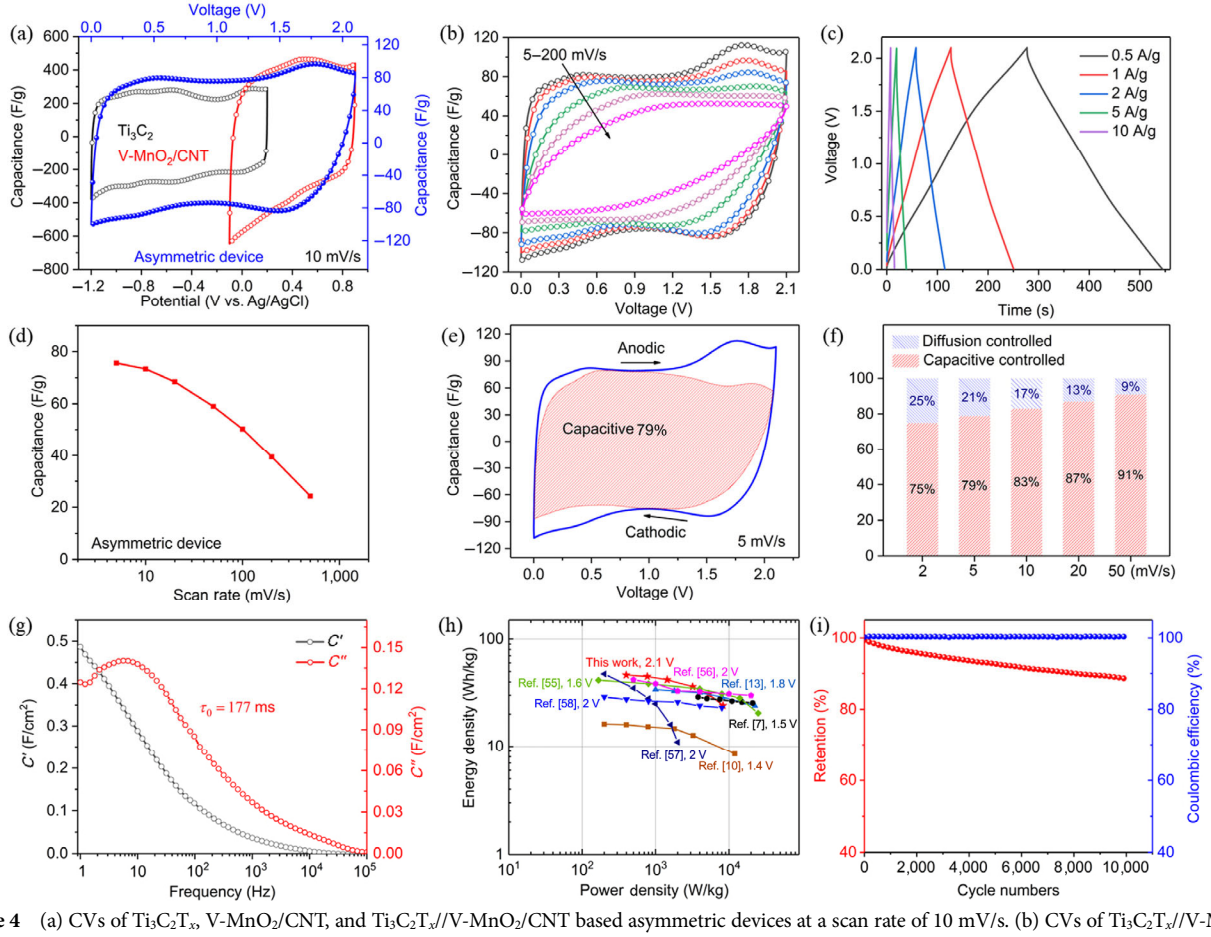

Figure 4 (a) CVs of $Ti_3C_2T_x$, V-MnO_2/CNT, and $Ti_3C_2T_x$//V-MnO_2/CNT based asymmetric devices at a scan rate of 10 mV/s. (b) CVs of $Ti_3C_2T_x$//V-MnO_2/CNT asymmetric device at different scan rates. (c) Galvanostatic charge–discharge curves of asymmetric device at different current densities. (d) Specific capacitance of asymmetric device at different scan rates. (e) The capacitive controlled within tested device at 5 mV/s. (f) The contribution of capacitive and diffusion-controlled current at different scan rates. (g) Normalized real (C') and imaginary (C'') parts of capacitance vs. frequency of the device. (h) Ragone plot displaying a real energy and power densities of $Ti_3C_2T_x$//V-MnO_2/CNT asymmetric device. (i) Cycling stability and Coulombic efficiency of the asymmetric device over 10,000 cycles in 1 M Li_2SO_4 electrolyte at a scan rate of 50 mV/s.

3 Conclusion

In conclusion, an asymmetric supercapacitor was successfully assembled using a MXene-based negative and V-MnO_2-based positive and tested in Li_2SO_4 electrolyte. This device exhibited an expanded operation voltage window of 2.1 V, resulting in a maximum energy density of 46 Wh/kg. This device still delivered a high energy density of 36 Wh/kg at a power density of 3.2 kW/kg. Additionally, this cell demonstrated a good cycling stability with a capacitance retention of 92% after 5,000 cycles. This study establishes the possibility of using asymmetric MXene-based hybrid devices to expand the working voltage window of traditional redox-capable materials in aqueous electrolytes.

4 Experimental section

4.1 Synthesis of $Ti_3C_2T_x$ MXene

$Ti_3C_2T_x$ MXene was synthesized following previously reported procedure [49]. 60 mL of 12 M HCl (Sigma Aldrich), 50% HF (Acros), and deionized (DI) water in a volumetric ratio of 6:1:3, respectively, was prepared as the etchant. 3 g Ti_3AlC_2 MAX powder with mesh size ≤ 40 μm (Carbon-Ukraine, Kiev, Ukraine) was slowly added into the etchant solution, and stirred on a hot plate at 35 °C for 24 h. The multilayer (ML) $Ti_3C_2T_x$ MXene was washed with DI water by centrifugation at 3,500 rpm until a pH of ≈ 6 was reached. Then, the ML $Ti_3C_2T_x$ was delaminated using 3 g of LiCl (Sigma Aldrich) in 50 mL of DI water and stirred for 4 h. This mixture was then repeatedly washed with DI water and then centrifuged at 3,500 rpm for 10 min cycles. After each cycle, the supernatant (if clear) was discarded, and the sediment was redispersed in fresh DI water. Once the supernatant was black, the mixture was then centrifuged for 1 h at 3,500 rpm, with the resultant supernatant discarded and the sediment redispersed in fresh DI water. After 6 cycles of 1 h, the mixture was then centrifuged for 10 min, with the resultant black supernatant collected. The decanted suspension was then vacuum filtered on a Celgard membrane to get the free-standing $Ti_3C_2T_x$ film which was used as the cathode/negative electrode.

4.2 Synthesis of the V-MnO_2 electrodes

V-MnO_2 was prepared following our previous report [50]. $MnSO_4{\cdot}H_2O$, $(NH_4)_2SO_4$ and $(NH_4)_2S_2O_8$ (Sinopharm Chemical Reagent, China) were added into 40 mL deionized water in a 1:2:1 molar ratio, respectively. Then, 0.5 mmol NH_4VO_3 (Sinopharm Chemical Reagent, China) was added in the solution and stirred for 10 min at room temperature. After that, the solution was placed in a 50 mL stainless steel Teflon lined autoclave and treated hydrothermally at 140 °C for 12 h. After filtration and washing with deionized water 5 times, the resulting precipitate was dried at 80 °C under vacuum for 12 h, resulting in the V-doped α-MnO_2. The anode/positive composed of 70 wt.% V-MnO_2 powder and 30 wt.% CNT (Blue Nano, China). The solution (V-MnO_2 + CNT + DI water) was carried out by 1 h bath sonication followed by filtration and washing several times with deionized water. The resulting precipitate was dried at room temperature to obtain the free-standing films of the V-MnO_2-CNT electrode with the thickness of 20 μm.

4.3 Characterization

The microstructural properties of the electrode materials were characterized by XRD using Cu Kα radiation (λ = 1.5418 Å, Philips X' Pert Pro), field-emission SEM (FE-SEM, FEI Nova 450 Nano, 10 kV), TEM (HRTEM, TITAN, G2 60-300, 300 kV, equipped with an EDS detector, and XPS (AXIS-ULTRA DLD-600W). Infrared spectroscopy (IR) of the materials was performed on a VERTEX 70 (Bruker) FT-IR spectrometer over the wavenumber range of 400–4,000 cm^{-1} with KBr pelletisation. Raman analysis was performed on a LabRAM HR800 (Horiba Jobin Yvon) with a 532 nm illuminant.

4.4 Electrochemistry

The electrochemical performance of the devices was carried out using cyclic voltammetry, galvanostatic charging/discharging, and electrochemical cycling on a VMP300 electrochemical workstation (BioLogic, France). For all electrochemical measurements, the testing setup was a plastic Swagelok cell. In a three-electrode setup, $Ti_3C_2T_x$ and V-MnO_2/CNT were used as the working electrode, over-capacitive activated carbon films (≈ 100 μm, YP-50, Kuraray, Japan) were used as the counter electrode, and Ag/AgCl was used as the reference electrode. In an asymmetric device, $Ti_3C_2T_x$ was used as the negative and V-MnO_2/CNT was used as the positive electrode. For these tests, glassy carbon electrodes were used as current collectors and a polypropylene membrane (Celgard, USA) was used as the separator. The gravimetric capacitance (C_g, F/g) values were calculated using the following equation

$$C_g = \frac{1}{Vmv}\int i dV$$

where i is the current (mA), V is the potential window (V), v is the scan rate (mV/s), and m is the mass of the active material (mg), for two-electrode configuration (device measurements), and m is the mass of the active electrode materials in both electrodes (mg).

Gravimetric energy and power densities were calculated using the following equations

$$E_g = \frac{1}{m}\int iVdt$$

$$P_g = \frac{E_g}{\Delta t}$$

where m is the mass of the active electrode materials in both electrodes (mg), and Δt is the discharge time.

Impedance spectra: The real (C') and imaginary (C'') parts of capacitances were calculated using the following equations

$$C' = \frac{-Z''}{2\pi f A|Z|^2}$$

$$C'' = \frac{-Z'}{2\pi f A|Z|^2}$$

where $|Z|$ is the absolute value of impedance (Ω), Z' and Z'' are the real and imaginary components of impedance; f is the frequency (Hz); A is the geometrical footprint area of the device.

In the manufactured devices, we further quantified the capacitive contribution to the total current using the following relationship

$$i(V) = k_1 v + k_2 v^{0.5}$$

where v is the scan rate (mV/s), and $k_1 v$ and $k_2 v^{0.5}$ represent the currents from surface capacitance contribution and the diffusion-controlled Faradaic processes, respectively. So, k_1 and k_2 can be derived from the linear plot of $i(V)/v^{0.5}$ vs. $v^{0.5}$ with different scan rates.

Acknowledgements

This work was financially supported by the National Natural Science Foundation of China (Nos. 51972124, 51902115, and 51872101). Research reported in this publication was also supported by King Abdullah University of Science and Technology (KAUST) under the KAUST-Drexel Competitive Research Grant (No. OSR-CRG2016-2963 sub 11206). The authors express their gratitude to late Prof. J. Zhou for valuable discussions. The authors thank to the facility support of the Center for Nanoscale Characterization & Devices, WNLO-HUST and the Analysis and Testing Center, HUST.

Electronic Supplementary Material: Supplementary material (supplementary crystal structures of the V-MnO_2 and its SEM images, XPS and Raman spectroscopy measurements, Nyquist plots and CV measurements) is available in the online version of this article at https://doi.org/10.1007/s12274-021-3513-x.

References

[1] Simon, P.; Gogotsi, Y. Materials for electrochemical capacitors. *Nat. Mater.* **2008**, *7*, 845–854.
[2] Gogotsi, Y.; Simon, P. True performance metrics in electrochemical energy storage. *Science* **2011**, *334*, 917–918.
[3] Simon, P.; Gogotsi, Y.; Dunn, B. Where do batteries end and supercapacitors begin? *Science* **2014**, *343*, 1210–1211.
[4] Huang, Y. L.; Zeng, Y. X.; Yu, M. H.; Liu, P.; Tong, Y. X.; Cheng, F. L.; Lu, X. H. Recent smart methods for achieving high-energy asymmetric supercapacitors. *Small Methods* **2018**, *2*, 1700230.
[5] Gogotsi, Y. Energy storage wrapped up. *Nature* **2014**, *509*, 568–569.
[6] Li, Q.; Wu, J. B.; Huang, L.; Gao, J. F.; Zhou, H. W.; Shi, Y. J.; Pan, Q. H.; Zhang, G.; Du, Y.; Liang, W. X. Sulfur dioxide gas-sensitive materials based on zeolitic imidazolate framework-derived carbon nanotubes. *J. Mater. Chem. A* **2018**, *6*, 12115–12124.
[7] Liu, P. G.; Gao, Y.; Tan, Y. Y.; Liu, W. F.; Huang, Y. P.; Yan, J.; Liu, K. Y. Rational design of nitrogen doped hierarchical porous carbon for optimized zinc-ion hybrid supercapacitors. *Nano Res.* **2019**, *12*, 2835–2841.
[8] Zhang, H. Z.; Liu, Q. Y.; Fang, Y. B.; Teng, C. L.; Liu, X. Q.; Fang, P. P.; Tong, Y. X.; Lu, X. H. Boosting Zn-ion energy storage capability of hierarchically porous carbon by promoting chemical adsorption. *Adv. Mater.* **2019**, *31*, 1904948.
[9] Augustyn, V.; Simon, P.; Dunn, B. Pseudocapacitive oxide materials for high-rate electrochemical energy storage. *Energy Environ. Sci.* **2014**, *7*, 1597–1614.
[10] Wang, S. P.; Zhao, X. L.; Yan, X. J.; Xiao, Z. W.; Liu, C. C.; Zhang, Y. J.; Yang, X. W. Regulating fast anionic redox for high-voltage aqueous hydrogen-ion-based energy storage. *Angew. Chem., Int. Ed.* **2019**, *58*, 205–210.
[11] Li, Z. X.; Ma, C.; Wen, Y. Y.; Wei, Z. T.; Xing, X. F.; Chu, J. M.; Yu, C. C.; Wang K. L.; Wang, Z. K. Highly conductive dodecaborate/MXene composites for high performance supercapacitors. *Nano Res.* **2020**, *13*, 196–202.
[12] Sun, S.; Rao, D. W.; Zhai, T.; Liu, Q.; Huang, H.; Liu, B.; Zhang, H. S.; Xue, L.; Xia, H. Synergistic interface-assisted electrode-electrolyte coupling toward advanced charge storage. *Adv. Mater.* **2020**, *32*, 2005344.
[13] Sun, S.; Liu, B.; Zhang, H. S.; Guo, Q. B.; Xia, Q. Y.; Zhai, T.; Xia, H. Boosting energy storage via confining soluble redox species onto solid-liquid interface. *Adv. Energy Mater.* **2021**, *11*, 2003599.
[14] Wu, J. B.; Gao, X.; Yu, H. M.; Ding, T. P.; Yan, Y. X.; Yao, B.; Yao, X.; Chen, D. C.; Liu, M. L.; Huang, L. A scalable free-standing V_2O_5/CNT film electrode for supercapacitors with a wide operation voltage (1.6 V) in an aqueous electrolyte. *Adv. Funct. Mater.* **2016**, *26*, 6114–6120.
[15] Kong, L. P.; Zhang, C. F.; Wang, J. T.; Qiao, W. M.; Ling, L. C.; Long, D. H. Free-standing T-Nb_2O_5/graphene composite papers with ultrahigh gravimetric/volumetric capacitance for Li-ion intercalation pseudocapacitor. *ACS Nano* **2015**, *9*, 11200–11208.
[16] Jiang, Q.; Kurra, N.; Alhabeb, M.; Gogotsi, Y.; Alshareef, H. N. All pseudocapacitive MXene-RuO_2 asymmetric supercapacitors. *Adv. Energy Mater.* **2018**, *8*, 1703043.
[17] Zhai, T.; Sun, S.; Liu, X. J.; Liang, C. L.; Wang, G. M.; Xia, H. Achieving insertion-like capacity at ultrahigh rate via tunable surface pseudocapacitance. *Adv. Mater.* **2018**, *30*, 1706640.
[18] Sun, S.; Zhai, T.; Liang, C. L.; Savilov, S. V.; Xia, H. Boosted crystalline/amorphous $Fe_2O_{3-\delta}$ core/shell heterostructure for flexible solid-state pseudocapacitors in large scale. *Nano Energy* **2018**, *45*, 390–397.
[19] Zhang, X. Y.; Liu, X. Q.; Zeng, Y. X.; Tong, Y. X.; Lu, X. H. Oxygen defects in promoting the electrochemical performance of metal oxides for supercapacitors: Recent advances and challenges. *Small Methods* **2020**, *4*, 1900823.
[20] Boota, M.; Gogotsi, Y. MXene-conducting polymer asymmetric pseudocapacitors. *Adv. Energy Mater.* **2019**, *9*, 1802917.
[21] Huang, L.; Yao, X.; Yuan, L. Y.; Yao, B.; Gao, X.; Wan, J.; Zhou, P. P.; Xu, M.; Wu, J. B.; Yu, H. M. et al. 4-Butylbenzenesulfonate modified polypyrrole paper for supercapacitor with exceptional cycling stability. *Energy Storage Mater.* **2018**, *12*, 191–196.
[22] Huang, L.; Guo, Z. F.; Liu, K. S.; Xiong, L. K.; Huang, L. W.; Gao, X.; Wu, J. B.; Wan, J.; Hu, Z. M.; Zhou, J. Large-scale synthesis of size- and thickness-tunable conducting polymer nanosheets via a salt-templated method. *J. Mater. Chem. A* **2019**, *7*, 24929–24936.
[23] Yang, P. H.; Feng, C. Z.; Liu, Y. P.; Cheng, T.; Yang, X. L.; Liu, H. D.; Liu, K.; Fan, H. J. Thermal self-protection of zinc-ion batteries enabled by smart hygroscopic hydrogel electrolytes. *Adv. Energy Mater.* **2020**, *10*, 2002898.
[24] Zhu, S. J.; Li, L.; Liu, J. B.; Wang, H. T.; Wang, T.; Zhang, Y. X.; Zhang, L. L.; Ruoff, R. S.; Dong, F. Structural directed growth of ultrathin parallel birnessite on β-MnO_2 for high-performance asymmetric supercapacitors. *ACS Nano* **2018**, *12*, 1033–1042.
[25] Jia, H. A.; Cai, Y. F.; Lin, J. H.; Liang, H. Y.; Qi, J. L.; Cao, J.; Feng, J. C.; Fei, W. D. Heterostructural graphene quantum dot/MnO_2 nanosheets toward high-potential window electrodes for high-performance supercapacitors. *Adv. Sci.* **2018**, *5*, 1700887.
[26] Hu, Z. M.; Chen, M.; Zhang, H.; Huang, L.; Liu, K. S.; Ling, Y. S.; Zhou, H.; Jiang, Z.; Feng, G.; Zhou, J. Stabilization of layered manganese oxide by substitutional cation doping. *J. Mater. Chem. A* **2019**, *7*, 7118–7127.
[27] Wu, Z. S.; Winter, A.; Chen, L.; Sun, Y.; Turchanin, A.; Feng, X. L.; Müllen, K. Three-dimensional nitrogen and boron co-doped graphene for high-performance all-solid-state supercapacitors. *Adv. Mater.* **2012**, *24*, 5130–5135.
[28] Yu, P. P.; Zhang, Z. M.; Zheng, L. X.; Teng, F.; Hu, L. F.; Fang, X. S. A novel sustainable flour derived hierarchical nitrogen-doped porous carbon/polyaniline electrode for advanced asymmetric supercapacitors. *Adv. Energy Mater.* **2016**, *6*, 1601111.
[29] Zhang, X. Y.; Hou, L. L.; Ciesielski, A.; Samorì, P. 2D materials beyond graphene for high-performance energy storage applications. *Adv. Energy Mater.* **2016**, *6*, 1600671.
[30] Shao, Y. L.; El-Kady, M. F.; Sun, J. Y.; Li, Y. G.; Zhang, Q. H.; Zhu, M. F.; Wang, H. Z.; Dunn, B.; Kaner, R. B. Design and mechanisms of asymmetric supercapacitors. *Chem. Rev.* **2018**, *118*, 9233–9280.
[31] Song, X. L.; Wang, H.; Jin, S. M.; Lv, M.; Zhang, Y.; Kong, X. D.; Xu, H. M.; Ma, T.; Luo, X. Y.; Tan, H. F. et al. Oligolayered $Ti_3C_2T_x$ MXene towards high performance lithium/sodium storage. *Nano Res.* **2020**, *13*, 1659–1667.
[32] Xia, Y.; Mathis, T. S.; Zhao, M. Q.; Anasori, B.; Dang, A. L.; Zhou, Z. H.; Cho, H.; Gogotsi, Y.; Yang, S. Thickness-independent capacitance of vertically aligned liquid-crystalline MXenes. *Nature* **2018**, *557*, 409–412.
[33] Naguib, M.; Kurtoglu, M.; Presser, V.; Lu, J.; Niu, J. J.; Heon, M.; Hultman, L.; Gogotsi, Y.; Barsoum, M. W. Two-dimensional nanocrystals produced by exfoliation of Ti_3AlC_2. *Adv. Mater.* **2011**, *23*, 4248–4253.
[34] Halim, J.; Cook, K. M.; Naguib, M.; Eklund, P.; Gogotsi, Y.; Rosen, J.; Barsoum, M. W. X-ray photoelectron spectroscopy of select multi-layered transition metal carbides (MXenes). *Appl. Surf. Sci.* **2016**, *362*, 406–417.
[35] Hu, M. M.; Hu, T.; Li, Z. J.; Yang, Y.; Cheng, R. F.; Yang, J. X.; Cui, C.; Wang, X. H. Surface functional groups and interlayer water

determine the electrochemical capacitance of $Ti_3C_2T_x$ MXene. *ACS Nano* **2018**, *12*, 3578–3586.
[36] Zhang, C. F.; Kremer, M. P.; Seral-Ascaso, A.; Park, S. H.; McEvoy, N.; Anasori, B.; Gogotsi, Y.; Nicolosi, V. Stamping of flexible, coplanar micro-supercapacitors using MXene inks. *Adv. Funct. Mater.* **2018**, *28*, 1705506.
[37] Lukatskaya, M. R.; Mashtalir, O.; Ren, C. E.; Dall'Agnese, Y.; Rozier, P.; Taberna, P. L.; Naguib, M.; Simon, P.; Barsoum, M. W.; Gogotsi, Y. Cation intercalation and high volumetric capacitance of two-dimensional titanium carbide. *Science* **2013**, *341*, 1502–1505.
[38] Anasori, B.; Lukatskaya, M. R.; Gogotsi, Y. 2D metal carbides and nitrides (MXenes) for energy storage. *Nat. Rev. Mater.* **2017**, *2*, 16098.
[39] Luo, J. M.; Tao, X. Y.; Zhang, J.; Xia, Y.; Huang, H.; Zhang, L. Y.; Gan, Y. P.; Liang, C.; Zhang, W. K. Sn^{4+} ion decorated highly conductive Ti_3C_2 MXene: Promising lithium-ion anodes with enhanced volumetric capacity and cyclic performance. *ACS Nano* **2016**, *10*, 2491–2499.
[40] Huang, P. F.; Zhang, S. L.; Ying, H. J.; Yang, W. T.; Wang, J. L.; Guo, R. N.; Han, W. Q. Fabrication of Fe nanocomplex pillared few-layered $Ti_3C_2T_x$ MXene with enhanced rate performance for lithium-ion batteries. *Nano Res.* **2021**, *14*, 1218–1227.
[41] Ahmed, B.; Anjum, D. H.; Gogotsi, Y.; Alshareef, H. N. Atomic layer deposition of SnO_2 on MXene for Li-ion battery anodes. *Nano Energy* **2017**, *34*, 249–256.
[42] Xiong, D. B.; Li, X. F.; Bai, Z. M.; Lu, S. G. Recent advances in layered $Ti_3C_2T_x$ MXene for electrochemical energy storage. *Small* **2018**, *14*, 1703419.
[43] Bao, W. Z.; Shuck, C. E.; Zhang, W. X.; Guo, X.; Gogotsi, Y.; Wang, G. X. Boosting performance of Na-S batteries using sulfur-doped $Ti_3C_2T_x$ MXene nanosheets with a strong affinity to sodium polysulfides. *ACS Nano* **2019**, *13*, 11500–11509.
[44] Li, C.; Kota, S.; Hu, C.; Barsoum, M. W. On the synthesis of low-cost, titanium-based MXenes. *J. Ceram. Sci. Technol.* **2016**, *7*, 301–306.
[45] Shuck, C. E.; Sarycheva, A.; Anayee, M.; Levitt, A.; Zhu, Y. Z.; Uzun, S.; Balitskiy, V.; Zahorodna, V.; Gogotsi, O.; Gogotsi, Y. Scalable synthesis of $Ti_3C_2T_x$ MXene. *Adv. Eng. Mater.* **2020**, 22, 1901241.
[46] Alhabeb, M.; Maleski, K.; Anasori, B.; Lelyukh, P.; Clark, L.; Sin, S.; Gogotsi, Y. Guidelines for synthesis and processing of two-dimensional titanium carbide ($Ti_3C_2T_x$ MXene). *Chem. Mater.* **2017**, *29*, 7633–7644.
[47] Lukatskaya, M. R.; Kota, S.; Lin, Z. F.; Zhao, M. Q.; Shpigel, N.; Levi, M. D.; Halim, J.; Taberna, P. L.; Barsoum, M. W.; Simon, P. et al. Ultra-high-rate pseudocapacitive energy storage in two-dimensional transition metal carbides. *Nat. Energy* **2017**, *6*, 17105.
[48] Li, J. M.; Levitt, A.; Kurra, N.; Juan, K.; Noriega, N.; Xiao, X.; Wang, X. H.; Wang, H. Z.; Alshareef, H. N.; Gogotsi, Y. MXene-conducting polymer electrochromic microsupercapacitors. *Energy Storage Mater.* **2019**, *20*, 455–461.
[49] Levitt, A. S.; Alhabeb, M.; Hatter, C. B.; Sarycheva, A.; Dion, G.; Gogotsi, Y. Electrospun MXene/carbon nanofibers as supercapacitor electrodes. *J. Mater. Chem. A* **2019**, *7*, 269–277.
[50] Hu, Z. M.; Xiao, X.; Huang, L.; Chen, C.; Li, T. Q.; Su, T. C.; Cheng, X. F.; Miao, L.; Zhang, Y. R.; Zhou, J. 2D vanadium doped manganese dioxides nanosheets for pseudocapacitive energy storage. *Nanoscale* **2015**, *7*, 16094–16099.
[51] Zhao, D. Y.; Zhao, R. Z.; Dong, S. H.; Miao, X. G.; Zhang, Z. W.; Wang, C. X.; Yin, L. W. Alkali-induced 3D crinkled porous Ti_3C_2 MXene architectures coupled with NiCoP bimetallic phosphide nanoparticles as anodes for high-performance sodium-ion batteries. *Energy Environ. Sci.* **2019**, *12*, 2422–2432.
[52] Natu, V.; Benchakar, M.; Canaff, C.; Habrioux, A.; Célérier S.; Barsoum, M.W. A critical analysis of the X-ray photoelectron spectra of $Ti_3C_2T_z$ MXenes. *Matter* **2021**, *4*, 1224–1251.
[53] Lukatskaya, M. R.; Dunn, B.; Gogotsi, Y. Multidimensional materials and device architectures for future hybrid energy storage. *Nat. Commun.* **2016**, *7*, 12647.
[54] Wang, J.; Polleux, J.; Lim, J.; Dunn, B. Pseudocapacitive contributions to electrochemical energy storage in TiO_2 (Anatase) nanoparticles. *J. Phys. Chem. C* **2007**, *111*, 14925–14931.
[55] Shen, J. L.; Yang, C. Y.; Li, X. W.; Wang, G. C. High-performance asymmetric supercapacitor based on nanoarchitectured polyaniline/graphene/carbon nanotube and activated graphene electrodes. *ACS Appl. Mater. Interfaces* **2013**, *5*, 8467–8476.
[56] Su, F. H.; Miao, M. H. Asymmetric carbon nanotube-MnO_2 two-ply yarn supercapacitors for wearable electronics. *Nanotechnology* **2014**, *25*, 135401.
[57] Jiang, H.; Li, C. Z.; Sun, T.; Ma, J. A green and high energy density asymmetric supercapacitor based on ultrathin MnO_2 nanostructures and functional mesoporous carbon nanotube electrodes. *Nanoscale* **2012**, *4*, 807–812.
[58] Cheng, Y. W.; Zhang, H. B.; Lu, S. T.; Varanasi, C. V.; Liu, J. Flexible asymmetric supercapacitors with high energy and high power density in aqueous electrolytes. *Nanoscale* **2013**, *5*, 1067–1073.